Advanced Robotics Research

ADVANCED ROBOTICS RESEARCH Open Access

RESEARCH ARTICLE OPEN ACCESS

Miniaturized Magnetic Tip Design for Endoluminal Vine Robot Navigation

Andrea Yanez Trujillo | Joshua Davy | James H. Chandler | James Avery | Pietro Valdastri

STORM Lab, School of Electronic and Electrical Engineering, University of Leeds, Leeds, United Kingdom

Correspondence: Andrea Yanez Trujillo (el23alyt@leeds.ac.uk)

Received: 31 October 2025 | **Revised:** 13 January 2026 | **Accepted:** 14 January 2026

Keywords: endoluminal navigation | magnetic actuation | soft growing robots | surgical robotics | vine robots

ABSTRACT

Minimally invasive surgery relies on tools that can access deep into delicate anatomy without causing harm, but traditional rigid instruments often struggle in these environments. Soft-growing, or "vine" robots, minimize tissue stress by extending from the tip instead of translating. However, their continuously changing tip material makes steering while carrying distal payloads such as cameras or sensors challenging. This work introduces a 7 mm soft-growing robot with a permanent magnet-based tip mount for wireless magnetic steering while preserving a 3 mm internal channel for tool deployment. The compact internal–external ring magnet (IRM–ERM) assembly accommodates a 1 mm RGB camera and 0.5 mm LED for live imaging. A systematic design study balanced growing pressure, $P_g \approx 20$ kPa, and magnetic attachment force, $F \approx 0.3$ N, across magnet geometries and separations, achieving stable operation. Workspace analysis demonstrated ±90° magnetic steering at varied lengths, and a 34 mm bending radius. Five target areas in the upper bronchial tree of a phantom were reached in an average of 35 ± 13 s per bifurcation. Compared with recent studies, this millimeter-scale platform combines miniaturization, magnetic control, onboard visualization, and working channel preservation. The selected steerable magnetic tip mount advances compact, multifunctional systems for endoluminal navigation.

1 | Introduction

Minimally invasive robotic surgery has transformed clinical practice by improving safety and reducing patient trauma, leading to faster recovery times with fewer complications [1]. However, platforms with traditional rigid manipulators, such as Intuitive Surgical da Vinci System, face challenges with elevated costs, high stiffness, and miniaturization, preventing their application in endoluminal interventions, opening a key area of research.

Recent developments in soft robotics have started to address these limitations by introducing highly compliant, bioinspired structures that support morphological adaptability [2]. The use of deformable soft materials has endowed robots with the capability to conform to delicate anatomical structures and navigate through natural body orifices, further reducing the need for incisions and lowering patient morbidity [3]. Among these, soft growing vine robots are unique because, instead of translating, they extend via tip growth through eversion, thereby minimizing stress on surrounding walls [4].

During eversion, the robot's thin-walled tubular body extends by turning inside out as the internal material is emitted from the tip when pressurized with air or liquid [5]. This ability to grow narrow profiles within confined spaces, along with their miniaturization potential, attracts significant research interest in endoluminal applications.

Lacking deliberate directional control, everting bodies have adopted compact steering mechanisms that enable vine robots to navigate dynamic environments [6]. For example, internal steering using rigid tendons through the inner lumen has been demonstrated [7]. Yet, this approach compromises compliance, obstructs the internal channel, and necessitates a duty cycle of

pressurization, growth, depressurization, and retraction of the tendon to synchronize growth. Alternatively, cable-driven actuation mechanisms bend the body by pulling cables routed along the wall of the vine [8, 9], and soft pneumatic actuators as pouch motors [10] or pneumatic artificial muscles (PAMs) [8, 11–14], provide smoother bending through selective pressurization. Nevertheless, despite their cost-effectiveness, the manufacturability of these types of actuators becomes complex at small scales, and their curvature control is limited when navigating successive bifurcations without accurate tip positioning.

Magnetic actuation has emerged as a promising solution for wireless steering of vine robots using embedded magnets controlled by external magnetic fields [15]. This remote operation facilitates miniaturization by removing bulky internal actuators, yet scaling down to millimeter diameters depends on ensuring sufficient magnetic volume. Davy et al. introduced fully soft 4–8 mm magnetic vine robots (MVR) with magnetic microparticles embedded in a silicone skin layer [16] and magnetic fluid to allow steering through the airways using external permanent magnets (EPMs) [17]. Directional control, however, was only possible with close proximity to the EPMs because the reduced magnetic volumes yield low magnetic moments that require high external magnetic fields, which may be impractical in clinical settings. The magnetic moments can be increased by using small permanent magnets. Watson et al. [18] demonstrated a 12 mm robot for sensing localization with an internal ring magnet (IRM) at the tip, enabling the vine to evert through its center, while leaving the lumen free for tool passage. Although the ring represents a high magnetic moment, the downside is its rigidity, which can limit the tip's flexibility.

Affixing cameras or sensors at the tip of a growing robot is also difficult because of the continuously changing material that everts from within [5]. Tethered caps have been proposed for secure attachment [4, 19], but internal objects are subject to the well-known "spitting problem", where the internal material advances at twice the tip speed, pushing objects forward and ejecting them [20]. To mitigate this, internal pressurization of the vine's central lumen has proved to counteract squeezing forces, allowing strings or cables to run freely without friction [21].

On the other hand, mounting tools directly on a tip cap attached solely by friction is another approach [10], but risks detachment and inhibits the robot's ability to shrink through confined spaces or gaps [21]. An alternative is a soft fabric cap that increases friction without compromising compliance [22]. However, this still obstructs the lumen and is susceptible to detachment during retraction. Improved solutions use small, free-spinning, ring magnets that slide with the material during growth [23, 24]. Nonetheless, this mechanism complicates manufacturing at smaller scales.

Recent studies aim to translate vine robots into clinical applications, such as colonoscopy [25, 26], combining growth, steering, imaging, and retraction in single devices. Although these systems demonstrate clinical feasibility, their diameters remain large (18–25 mm D_b), and the working channel is often obstructed by tip mounts. More compact designs, such as Vine4Spine [27], have been miniaturized to 2 mm while integrating a 1.2 mm multilumen catheter. However, the use of a NiTi tendon for actuation increases body stiffness and complicates growth synchronization. Additionally, incorporating the endoscope and sensors within the catheter reduces the available tool channel to only 0.24 mm, restricting the range of tools that can be delivered.

Prior studies have managed to integrate continuous growth, active steering, and onboard imaging, but not into a millimeter-scale design that preserves body flexibility and a sufficiently large working channel [28]. This limits the essential delivery of tools or suction to smaller endoluminal environments. In this work, we present a methodology for the systematic design and evaluation of a miniaturized magnetic tip mount that balances magnetic coupling and low eversion resistance. We verify the design through the derivation and modeling of the primary magnetic and growing forces involved. Based on this derivation, we developed a tip design for a 7 mm vine robot that integrates a compact internal–external ring magnet (IRM–ERM) configuration for wireless magnetic steering, while maintaining a 3 mm working channel, and an onboard RGB camera with LED illumination for simultaneous tool passage and visualization (Figure 1). We further analyze the workspace and performance of the proposed robot design in open-space and simple navigation tasks. Finally, we validated the system through endoluminal exploration within a bronchial phantom to reach five target areas in the upper bronchial tree.

2 | System Design

The challenge of integrating active steering, tethered imaging, payload capacity, and an active working channel within a soft, everting body is significantly amplified when aiming for miniaturization. Addressing these essential capabilities individually introduces mechanical trade-offs that complicate the design

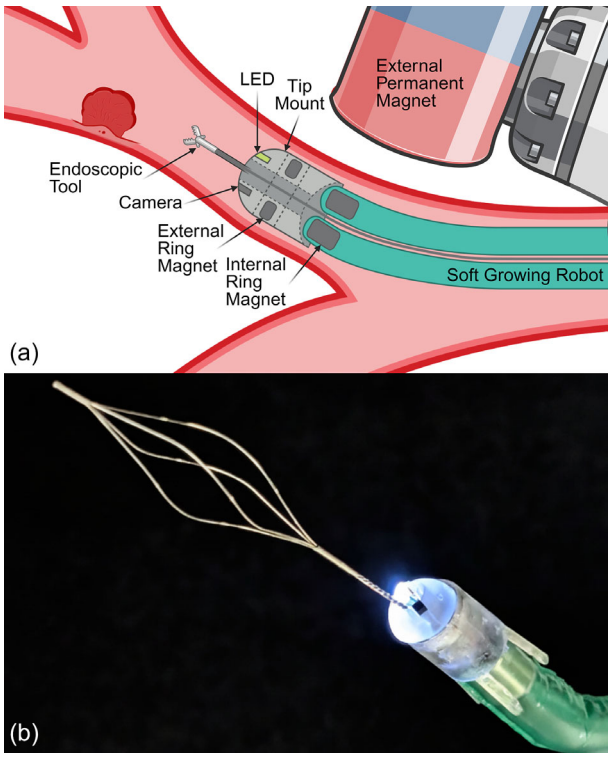

FIGURE 1 | (a) Schematic of the soft growing robot with magnetic tip mount. (b) A prototype tip mount with integrated camera and LED. An endoscopic tool deploys from the 3 mm instrument channel.

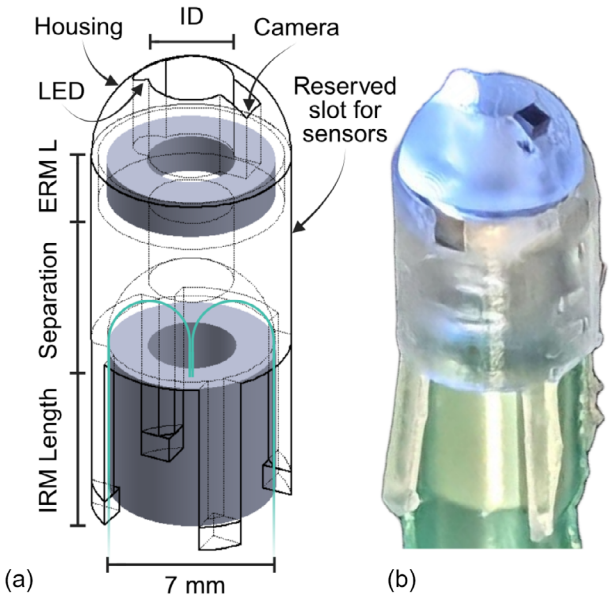

FIGURE 2 | (a) Schematic showing the IRM–ERM configuration, highlighting variable parameters: internal diameter (ID), length (L), and separation. (b) Assembled prototype of the tip mount.

and limit scalability. Therefore, to ensure that the system could support endoluminal navigation, the tip design is guided by parameters from comparable endoscopes. Specifically, the design should provide deliberate directional control (at least ±90°), accommodate onboard imaging and additional payload capacity while ensuring that the minimum growing pressure remains safely below the burst pressure, preserve the lumen as an unobstructed 2.2–3.6 mm working channel for tool deployment, and remain sufficiently small (typical body diameters range between 5 and 7 mm) and compliant to preserve the flexibility of the soft everting body [3, 29]. Consequently, our design approach emphasizes simplicity of functional integration. In this regard, the miniaturization possibilities offered by wireless magnetic actuation are leveraged to consolidate all functions into a compact magnetic tip. As shown in Figure 2, the design comprises an IRM magnetically coupled to an external ring magnet (ERM) housed within a mount at the tip of the vine body.

2.1 | Vine Body Fabrication

A body diameter of 7 mm was identified as a diameter that provides sufficient space for a continuous 3 mm working channel, while also accommodating the magnetic ring assembly and the onboard camera, and LED. At this scale, the robot was experimentally demonstrated to grow to lengths of ≈400 mm, making it suitable for navigation in distal luminal anatomy. This diameter was therefore selected for fabrication, ensuring the design achieves the smallest feasible size without compromising operational capabilities.

The tubular body is constructed from two laser-cut thin films of Thermoplastic Polyurethane (TPU) (Stretchlon 200, Airtech Advanced Materials, UK), each 38 μm thick. Following the fabrication process in [17], the layers are heat-pressed (Combo Heat Press, Creworks, USA) at 100°C for 120 s to seal them into close contact, before laser-cutting to the external geometry at 2733 mm min^{-1} speed and 50% laser power (Creality Falcon 2 Pro 22 W, Creality, China).

2.2 | Magnetic Tip Mount

A miniature magnetic tip mount is embedded to enable wireless steering (Figure 2). The internal part consists of an internal ring magnet (IRM), which provides sufficient magnetic volume for reliable actuation at a distance without introducing friction to the environment. An external cap incorporates an external ring magnet (ERM) to magnetically interlock with the IRM, securing both at the tip and enabling the carrying of payloads.

The proposed ring-based design maintains an open conduit to the tip, preserving external access to the intrinsic working channel of the vine robot lumen for endoscopic tools. Additionally, to mitigate the IRM–ERM interaction, which increases friction on the everting skin due to their magnetic force, the two magnets are separated by a 3D-printed tip housing (Clear Resin V4, Formlabs, USA). Furthermore, this housing can also serve to accommodate imaging, sensors, or tools, while preserving a 3 mm working channel.

2.3 | Tip Modeling

In order to understand the design requirements, we develop a simplified model to account for the additional load from the tip mount during growth. Under quasistatic conditions, the growing force F_g is generated by the internal pressure P_g acting over the vine body cross-sectional area $A_b = \pi D_b^2/4$, ($D_b = 7$ mm), overcoming both path-independent and dependent losses (Equation 1) [30].

$$F_g = P_g A_b = \underbrace{[F_Y + F_v]}_{\text{Path-Independent}} + \underbrace{\left[F_l + \sum_i F_{Ci}\right]}_{\text{Path-Dependent}} \tag{1}$$

where F_Y is the yield force required to initiate growth, and F_v, F_l, F_{Ci} are the velocity-, length-, and curvature-dependent force terms, respectively. When a tip mount is added, an additional load appears at the distal end, requiring a higher pressure P_g^{tip}, and thus higher force F_g^{tip}, for eversion (Equation 2).

$$F_g^{tip} = P_g^{tip} A_b = F_g + F_{tip} \tag{2}$$

The resulting increase in pressure corresponds to the tip force F_{tip}, which is proportional to the pressure difference (Equation 3).

$$F_{tip} = (P_g^{tip} - P_g) A_b \tag{3}$$

This resistance originates primarily from friction between the everting membrane and the magnetic mount, which opposes motion in proportion to the magnetic normal force N_{mag} (Equation 4).

$$F_{tip} = \mu_{apparent} N_{mag} \tag{4}$$

where $\mu_{apparent}$ represents an effective friction coefficient between the TPU vine membrane and the IRM–ERM housing that

accounts for material friction and eversion effects (e.g., membrane deformation and sliding over the IRM–ERM assembly). The latter is captured by the magnetically induced eversion resistance F_{ev}, which arises from magnetic interactions that modify eversion dynamics. This is proportional to the correction factor k_{ev} that scales the intrinsic material friction component F_f (Equation 5).

$$F_{tip} = F_f + F_{ev} = F_f + k_{ev} F_f = (1 + k_{ev}) F_f \tag{5}$$

Considering Coulomb friction $F_f = \mu N_{mag}$, where μ is the material friction coefficient between the TPU membrane and the 3D-printed housing, the compact analytical form can be expressed as (Equation 6):

$$F_{tip} = (1 + k_{ev}) \mu N_{mag} = \kappa \mu N_{mag} \tag{6}$$

where $\kappa = 1 + k_{ev}$ denotes the combined friction-eversion coefficient linking the tip force to magnetic loading. Finally, to calculate P_g^{tip}, (Equation 3) is replaced into (Equation 6) to obtain (Equation 7):

$$P_g^{tip} = (\kappa \mu N_{mag} / A_b) + P_g \tag{7}$$

3 | Experimental Design Study

The use of the IRM and ERM at the tip enables magnetic steering and payload capacity but introduces a trade-off between magnetic coupling and eversion resistance. Specifically, the IRM geometries and IRM–ERM magnetic force add frictional resistance that affects the eversion process and requires characterization. Also, a greater separation between the magnets can reduce the magnetic force and thus the friction, but also risks failing to hold the mount securely in place. A suitable design configuration should therefore balance the minimum pressure at which growth starts with sufficient magnetic attachment.

The minimum pressure required to initiate growth is an important indicator of a vine robot's performance [23]. Because the maximum operating pressure is limited by the body's burst pressure, any increase in friction raises the minimum growing pressure and narrows the operating range. Since the tip mount introduces new contact surfaces that resist the everting motion, we investigated its impact by conducting horizontal growth experiments. With slack left in the tail to allow unconstrained forward movement, pressure was gradually increased until growth started, and the value at which the tip first began to extend was recorded as the minimum pressure. Each test was repeated five times per configuration, and results are reported as mean ± standard deviation to account for variability.

3.1 | IRM

The influence of introducing an internal ring on the minimum growing pressure has not been previously reported. Different IRM geometries represent different contact areas with the everting membrane, resulting in varied frictional resistance, as reflected in the measured minimum growing pressure. To characterize this effect in isolation, not considering yet the ERM, non-magnetized 3D-printed IRM prototypes (Gray Resin V4, Formlabs, USA) with varied internal diameters and lengths were evaluated alongside standard-sized axially magnetized ring magnets (NdFeB N42, K&J Magnetics, USA). A 6 mm outer diameter (OD) IRM prototype was fixed to fit inside the 7 mm vine, while the internal diameter (ID) ranged from 3 to 5 mm and the length from 1.5 to 6 mm, corresponding to thicknesses between 3 and 1 mm. Commercially available magnets of OD × ID of 6.3 × 3.2 mm were also tested at lengths of 1.5, 3.2, 4.7, and 6.3 mm (Figure 3a).

Figure 3b shows that, as expected, larger internal diameters allow the vine to grow at lower minimum pressures. Conversely, thinner IRMs permit growth at lower pressures, as less contact area creates lower frictional resistances. Likewise, increasing the IRM length also requires higher minimum growing pressures, although the impact is lower for the permanent magnets, likely due to a lower friction coefficient (Figure 3c). These results support selecting the largest possible ring magnet to maximize the magnetic moment without excessively increasing friction. Although thinner or smaller rings reduce the minimum growing pressure, their reduced magnetic volume restricts the steering capability at clinically relevant actuation distances. Consequently, the largest commercially available ring magnet was selected.

3.2 | ERM

Further experiments were conducted to characterize the effect of ERM geometry on the magnetic coupling between the IRM and ERM. Using the selected IRM configuration identified in the previous tests, ERMs with the same OD and ID were evaluated to isolate the influence of length and separation distance between magnets. Three ERM lengths (1.5, 3.2, and 6.3 mm) were selected to represent different magnetic moments. At the same time, the axial separation distance between the magnets was varied from 2 to 8 mm using custom 3D-printed housings (Gray Resin V4, Formlabs, USA) (Figure 3d). Reducing the separations is expected to increase magnetic force and attachment reliability but raise friction and minimum growing pressures, while larger separations would ease eversion but risk premature detachment. To mitigate this, ERM housings incorporating retaining legs to latch onto the IRM were also tested. The influence of the added friction during growth was quantified by measuring the minimum growing pressure for each configuration.

The results confirm a clear trade-off between magnetic coupling and ease of eversion. As illustrated in Figure 3e, reducing the separation between the IRM and ERM increases the magnetic force, but raises the minimum pressure required for eversion. At the smallest tested separation of 2 mm, growth is limited to relatively high pressures, while larger separations (6–8 mm) permit eversion at lower pressures but frequently lead to misalignment and premature detachment. Consistently, increasing the ERM length produces greater magnetic moments and thus increases magnetic forces, but at the cost of higher minimum pressures. Accordingly, the smallest possible ERM length of 1.5 mm was selected to minimize the tip weight and facilitate eversion. However, since this configuration is more prone to detachment, particularly during steering, the incorporation of retaining legs is further investigated through force measurements.

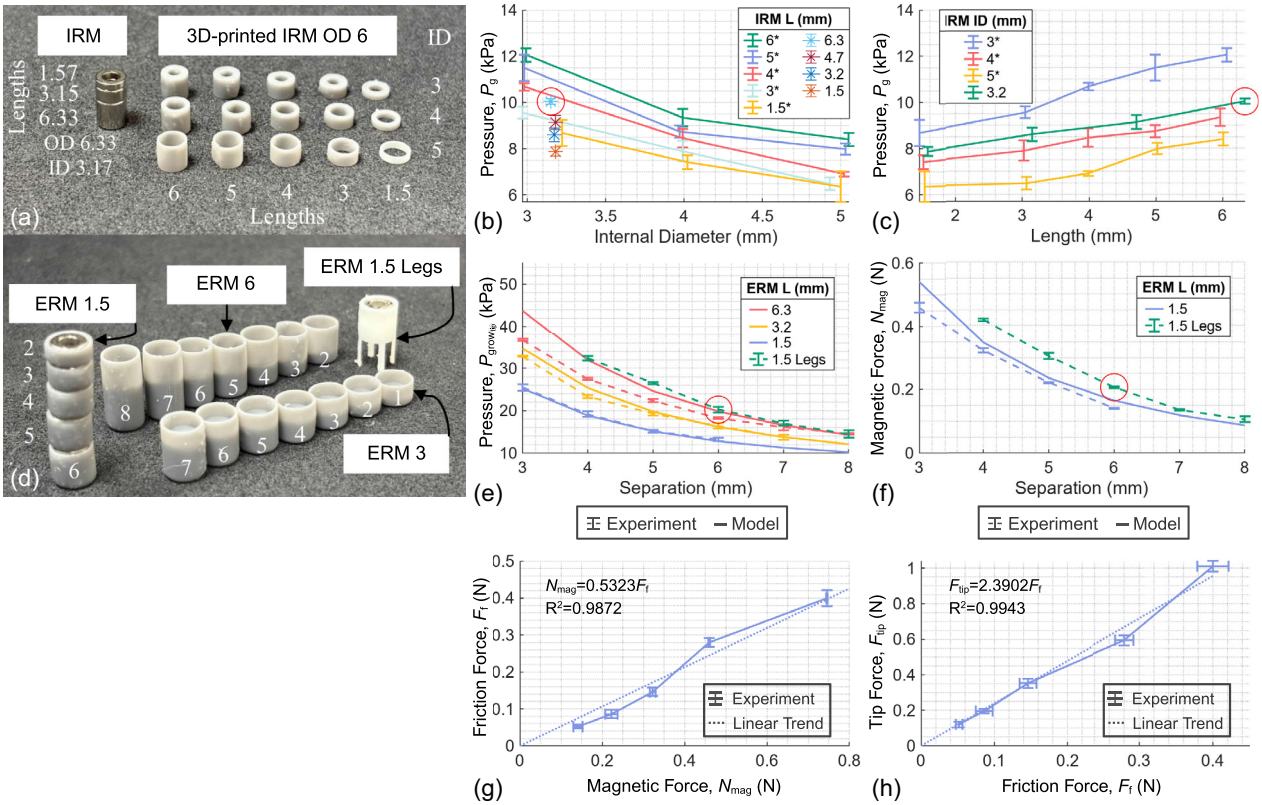

FIGURE 3 | Tip mount experimental design study with internal and external ring magnet (IRM–ERM) prototypes. (a–c) IRM prototypes and effect of internal diameter and length on minimum growing pressure. (d–f) ERM prototypes in housings with and without retaining legs, showing the impact of ERM length and IRM–ERM separation distance on growing pressure and magnetic force. Separations smaller than 3 mm caused excessive friction during eversion, preventing reliable growth. Housings without retaining legs could detach during growth at separations larger than 6 mm, improving to 8 mm when legs were added. (g–h) Independent experimental determination of coefficients $\mu = 0.5323$ and $k = 2.3902$ from linear fits used to parameterize the analytical model for tip friction and growing pressure prediction (in e–f). All 3D-printed IRMs used in (a–c) have OD = 6 mm; commercial IRMs and ERMs have OD = 6.3 and ID = 3.2 mm. *Asterisk indicates 3D-printed prototypes; all other sizes correspond to the ring magnets. Selected configurations are highlighted with red circles.

3.3 | IRM–ERM Magnetic Force

The magnetic force was measured through a pull test using a load cell (DBCR Compact S-Beam, Applied Measurements, UK) mounted vertically to a rigid frame. The IRM was fixed directly to the load cell via a threaded bolt, while the ERM, in its 3D-printed housing (Rigid 4000, Formlabs, USA), was manually pulled away in the axial direction until detachment. The load cell signal was recorded continuously, and the peak force immediately before separation was taken as the magnetic force. Each configuration was tested five times to report the mean and standard deviation, for both cases of ERM housings with and without retaining legs.

Incorporating legs can improve attachment by mechanically securing the ERM to the IRM carrier. As shown in Figure 3f, when the separation exceeds 6 mm, the legged mount design enables eversion at pressures well below the burst limit, thereby reducing the risk of detachment. This configuration provides the most practical balance between low growing pressure, for a reliable eversion, with sufficient magnetic force, for robust steering attachment, and is therefore selected as the most suitable configuration for subsequent navigation experiments.

To further evaluate attachment performance, the risk of mount being pulled off under external magnetic actuation was assessed by estimating the force exerted on the ERM by the EPM using dipole approximation with Magpylib [31]. Based on the EPM remanence value (1.40 T), the corresponding maximum field gradients at the 150 mm operational distance produce axial forces on the ERM of approximately ≈0.05 N. This remains an order of magnitude below the measured IRM–ERM pull-off force, F ≈ 0.3 N. Consistent with this estimate, no detachment was observed in any successive workspace or navigation experiments.

3.4 | Tip Model Validation

To validate the analytical tip model introduced in subsection 2.3, an experiment was conducted to quantify the coefficients (μ) and (k) in the magnetic tip force relation $F_{tip} = \kappa\mu\, N_{mag}$ (Equation 6). The setup consisted of pulling a segment of the everting membrane positioned between the IRM and the housing with ERM, while measuring the resulting frictional force with the load cell (DBCR Compact S-Beam, Applied Measurements, UK). By plotting this data against the magnetic normal force measured previously (Section 3.3), the friction coefficient $\mu = 0.5323$ was obtained through linear regression (Figure 3g). Subsequently, the total tip force, obtained from Equation (3), was plotted to extract the correction factor $k = 2.3902$ (Figure 3h), which

accounts for additional effects from eversion such as stretching or local deformation.

By substituting the experimentally derived coefficients in the tip model, we can predict the growing pressure with theoretical normal magnetic forces (N_{mag}) computed in Magpylib [31]. The simulation model replicated the IRM–ERM configuration used experimentally, defining the magnets' dimensions, magnetization, and relative separation gaps of 3–8 mm. Each magnet was modeled as an axially magnetized cylindrical segment with polarization values corresponding to the nominal remanence of the NdFeB material (1.05 T). The remanence was experimentally characterized by measuring the magnetic field at fixed distances using a tesla meter. The axial magnetic force between the IRM and ERM was computed over the range of separations. The resulting simulated normal magnetic force values are reported in Figure 3f, and the corresponding growing pressures in Figure 3e. The direct comparison to the experimental data validates the analytical tip model.

3.5 | Operating Range

For comparison, the minimum pressure required to begin growth by adding each portion of the design: inner ring magnet, outer cap, and full tip mount with IRM–ERM is plotted against the burst pressure limit (Figure 4). The results show that all tested configurations remain well below the experimentally measured burst pressure of the TPU body, defining an operating window for growth as the difference between the minimum pressure required to initiate growth and the burst pressure for each configuration. Adding the 6.3 mm IRM increases the minimum pressure by 58% (from 6.36 to 10.04 kPa). Mounting a 1.57 mm ERM cap with retaining legs at 6 mm separation from IRM further increases the pressure by an extra 102% (from 10.04 to 20.24 kPa). However, considering that the burst pressure is ≈55 kPa, the device reduces the operating range by 25% (from 48.64 to 34.76 kPa), comparable with a 24% reduction reported for an alternative cap design with magnetic rolling interlock [23].

Considering the path-dependent cumulative friction losses that increase with deployed length and curvature, maintaining a large operating window is critical because this range determines the remaining pressure margin available during deployment. Initiating growth at pressures near the burst limit would leave insufficient margin to compensate for these losses, restricting the complexity of feasible trajectories. Therefore, preserving this gap offers the possibility to apply higher pressures to traverse the complex anatomy, while increasing growing velocity and keeping the IRM securely at the tip during growth and steering, supporting the feasibility of the designed tip mount in subsequent navigation experiments.

4 | Experimental Evaluation

To validate the steering capabilities of the selected tip design under magnetic actuation, a workspace analysis was conducted to characterize the achievable bending angles. This analysis was followed by three experiments that evaluated the navigation possibilities through this method. Experiment 1 evaluates back-bending navigation with an obstacle. Experiment 2 studies navigation control around hoops in a three-dimensional space. Experiment 3 demonstrates navigation through a bronchial phantom.

4.1 | Workspace Analysis

For magnetic vine steering, the bending moment generated by the external magnetic fields must overcome the restoring moment of the everted body [15]. To investigate this capability with the miniaturized magnetic tip-mount design, the maximal bending that can be achieved in free space was characterized by defining the effective magnetic workspace of the robot.

The vine robot was pressurized to 25 kPa, everted to fixed lengths of 30, 60, and 90 mm, and positioned in free space. A 89 × 89 mm NdFeB N52 EPM (Magnetworld AG) was used for external magnetic field manipulation as the end effector of a 7-DOF serial

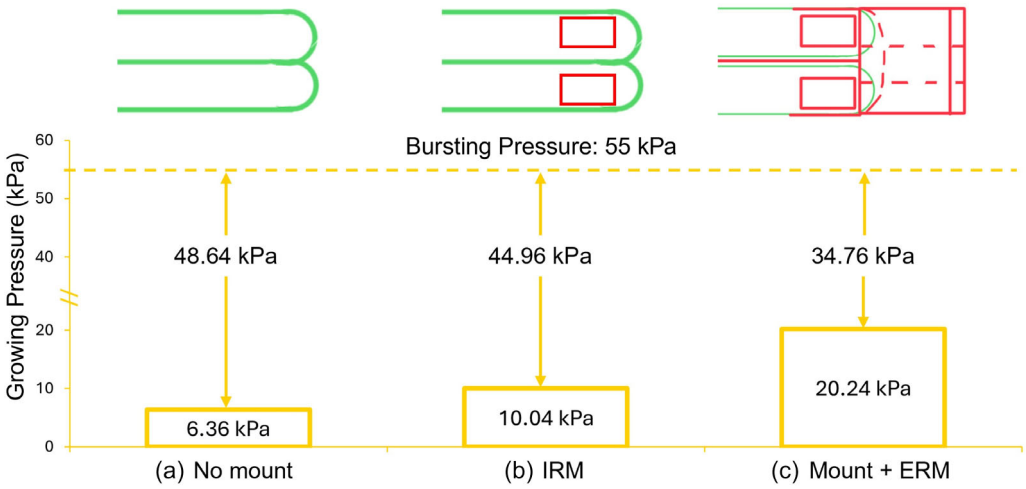

FIGURE 4 | The minimum pressure to start growth is compared against the experimentally measured burst pressure of the TPU body for each component added to the design: (a) no mount, (b) IRM, and (c) full IRM–ERM mount with retaining legs. All configurations remain well below the burst limit, reducing the operating range by 25% with the full mount but still leaving range for growth and steering.

robotic manipulator (14-kg payload LBR iiwa, KUKA, Germany). The KUKA arm was controlled via the joystick to adjust both Cartesian position and end-effector orientation, maintaining a constant 150 mm distance from the magnet center to the anchoring base. The resulting bending of the robot tip was tracked using overhead imaging, and the angle between the initial and deflected tip positions was extracted using image processing. The procedure was repeated across the full angular range of the end effector.

The measured workspace maps the applied EPM angle to the resulting robot tip angle under controlled EPM actuation. Figure 5 shows that the selected tip design achieved a wide range of bending angles when steering under EPM actuation. As the KUKA-mounted EPM is rotated around the tip, the robot tip angle follows the applied field direction by manipulating the end effector angle. Similar bending angles across different tested lengths suggest that magnetic actuation dominates over the restoring bending moment. The directional capability exceeds ±90°, indicating that the robot can cover a full semicircle in free space.

4.2 | Navigation

For the following navigation experiments, the same EPM was mounted on the robotic manipulator, controlled using a joystick to rotate the end effector around the robot tip to exert successive steering commands. Eversion was performed using a linear mechanical drivetrain that advanced with a programed button until the desired trajectories were completed. The robot's path was recorded using overhead video tracking, and corresponding timestamps were extracted for analysis.

4.2.1 | Experimental Setup

In traditional base assemblies, a sealed pressurized chamber enclosed a spooled mechanical drivetrain, preventing access to the vine robot's inner lumen. In our setup (Figure 6), inspired by Mammobot [7], the active inner channel and the surrounding annular space are accessed and pressurized independently. This configuration isolates the inner working channel for tool delivery while reserving the annular space for eversion.

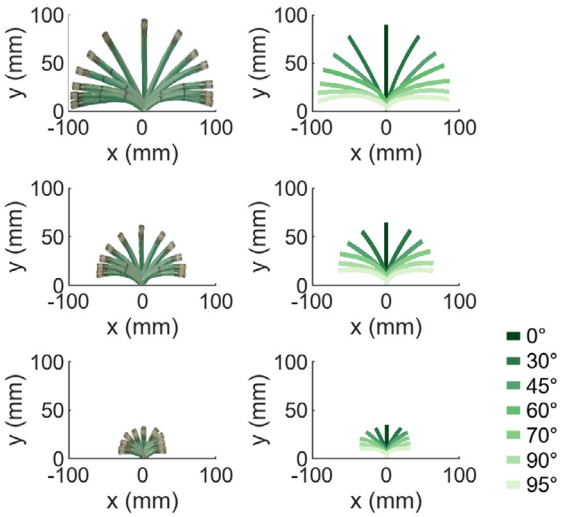

FIGURE 5 | Magnetic workspace analysis of the vine robot under EPM actuation for everted lengths of 30, 60, and 90 mm. The tip direction is measured under varying magnetic fields, demonstrating wide-angle directional capability beyond ±90° for navigating anatomical bifurcations.

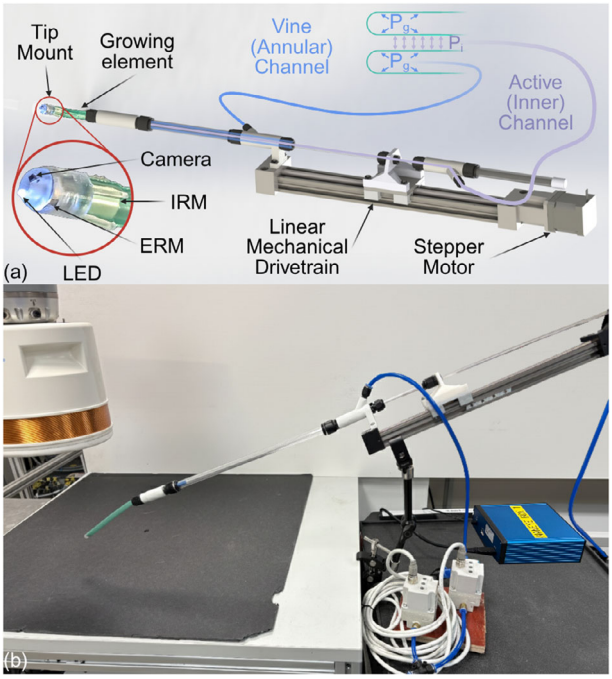

FIGURE 6 | Pneumatic base assembly for tool insertion. (a) Growth is achieved by independently pressurizing the active inner channel (P_i in green) and the annular external space (P_g in blue), while advancing a linear mechanical drivetrain. (b) Experimental setup for navigation.

Growth actuation is driven by programable pressure controllers (ITV1010-211BL, SMC, Japan) that regulate the inflation of the annular and inner channels, and a linear mechanical drivetrain (SAW-0630, IGUS, Germany), actuated by a stepper motor (NEMA 17, IGUS, Germany), that carries the active channel through a mobile support. This arrangement constrains the growing speed by applying pressure and simultaneously translating the active channel with a motor driver (S32, uStepper, Denmark) to release the tension on the vine, allowing the robot tip to evert. Custom 3D-printed adapters and clear acrylic tubes couple the vine body to the pressure lines (blue for growing pressure, P_g, and green for inner pressure, P_i), and drivetrain, while keeping the annular and inner chambers sealed.

4.2.2 | Onboard Tethered Imaging and Tool Deployment

In our work, pressure was applied in the internal working channel to equalize the annular pressure and allow the camera cable to advance at the same speed as the tip [21]. This balance of pressures, combined with light friction applied at the base of the cable to counteract residual friction, prevented the camera from being engulfed. As the IRM–ERM assembly is mounted around the inner channel rather than within the flow passage, the magnetic attachment remains secure.

A miniature NanEYE 1 × 1 mm camera (RGB CMOS, AMS-OSRAM, US) and white LED 1 × 0.5 mm (0402 SMD, Bright Components, UK) illumination were integrated into the mount

to enable onboard visualization. These components were positioned laterally within the tip mount to preserve the central lumen. As a result, the system delivered stable growth with the onboard payload while retaining the option to utilize the active channel for tool deployment (see Video S1).

4.2.3 | Back-Bending

In workspace analysis, the bending angle was limited by the robot's stiffness. However, backward bending requires a constraint that redirects the trajectory. In free space, the body can fold back on itself, but the bending is concentrated near the pivot point rather than forming a well-defined radius. Therefore, to test its ability to retroflect with magnetic steering, a cylindrical obstacle (25 mm radius) was used as a passive geometric guide, guiding the body to turn around it (Figure 7). Two reversal modes were demonstrated: steering while growing around the guide, and performing the turn after completing straight growth (see Supplementary Video 1). This setup enables bending with a constant radius, providing a reference for comparison with values reported by other actuation systems.

These experiments show that the robot can reverse direction around the cylindrical obstacle, completing trajectories of 155°. The measured turning radius to the vine centerline is ≈34 mm (Figure 7), which is larger than the 25 mm obstacle radius. The difference is likely due to the portions of the body locally buckling, which prevents smooth guidance along the obstacle surface. Instead, localized points bent more sharply near the contact point, including local buckling near the tip, which pivots slightly around the everting point, leading to a small offset between the vine tip direction and the applied magnetic field. These results demonstrate that obstacles can provide sufficient geometric support to enable turning. Accordingly, the magnetic tip could allow the vine robot to perform tight reversals in lumen-scale environments, as found in confined anatomical pathways.

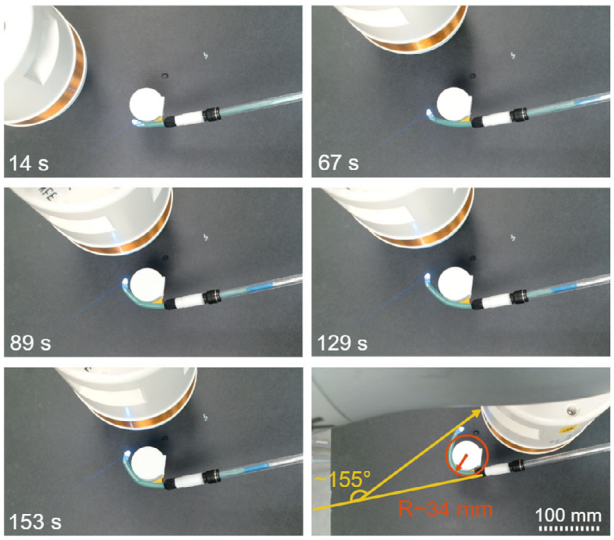

FIGURE 7 | Back-bending navigation under magnetic steering. The robot reverses direction around a cylindrical obstacle (25 mm radius) with a measured turning radius of ≈34 mm and angle of ≈155°. The larger radius compared to the obstacle is likely due to body buckling near contact regions, preventing smooth sliding along the surface.

4.2.4 | Hoop Navigation

To evaluate whether open-loop teleoperation could be effective in navigating more complex trajectories, 3D-printed hoops were used to shape paths that test the robot's maneuverability in three dimensions. The vine robot was everted through three consecutive vertical hoops with an internal diameter of 15 mm. The heights between the three hoops varied by 20 mm from one to the other, to create a reproducible 3D path. The same track was repeated five times (Figure 8).

The hoop navigation experiments indicate that the robot can follow successive 3D trajectories under open-loop magnetic steering. The vine completes a sequence of three hoops during smooth growth with an average time of 189 ± 26 s (see Video S1). Although the trajectory remains centered within the rings, slight deviations were observed during transitions between hoop segments. However, the robot consistently returns to the intended path, confirming that open-loop magnetic steering provides sufficient maneuverability to guide the robot in complex 3D geometries through lumen phantoms such as lung airway models.

4.2.5 | Phantom Navigation

Finally, five phantom experiments were carried out in a commercially available silicone surgical training simulator model of the human bronchial tree at anatomical scale (Ultrasonic Bronchoscopy Simulator, Adam Rouilly, UK) to validate magnetic steering in clinically relevant scenarios while maintaining clear video feedback with the NanEYE camera mounted at the tip. Again, EPM actuation was controlled via the joystick, while

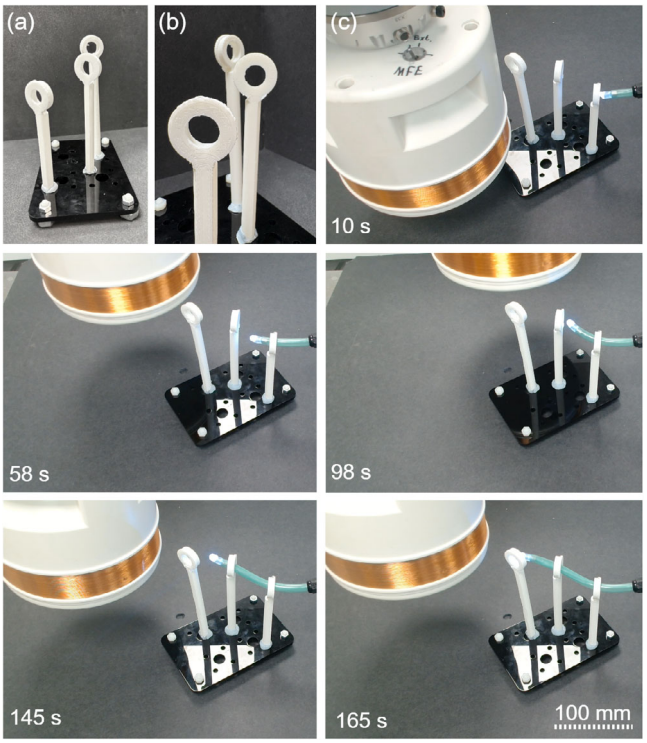

FIGURE 8 | Navigation through three consecutive hoops under open-loop magnetic steering. (a) General view and (b) robot view of the hoop structures, showing the 15 mm internal diameter rings, set at a height variation of 20 mm. (c) The robot was everted through the 3D hoop trajectory, completing five trials with an average time of 189 ± 26 s.

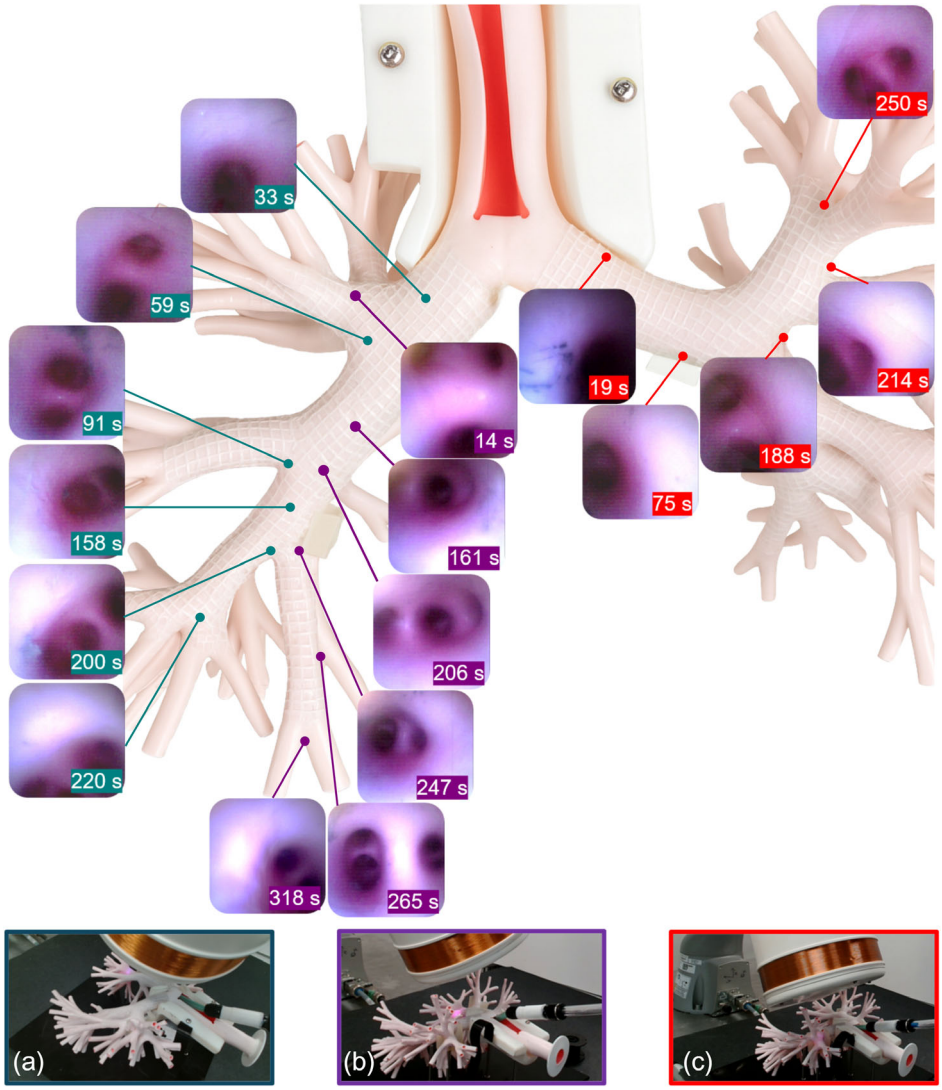

FIGURE 9 | Bronchial tree phantom navigation under magnetic steering. Three representative trajectories (a–c) are shown, with corresponding onboard camera views at bifurcations. In (a) and (b), the robot advanced through five successive bifurcations, while in (c) it traversed three, all reaching the tertiary bronchi.

eversion was actuated with the programed button. Unlike previous experiments, in this case, navigation was exclusively guided by the onboard camera, replicating the conditions of endoscopic procedures. The bifurcations and curved passages in the phantom represented a challenging scenario in which the operator relied only on the camera for guidance at branch points, without overhead vision. Between trajectories, the vine robot was manually removed from the phantom after completing each navigation, and reset to the initial configuration before redeployment. Both external and endoscopic views were recorded for evaluation.

The robot successfully navigated five trajectories, reaching the tertiary bronchi of the phantom. Three representative trajectories are illustrated in Figure 9. Videos of all trials are provided in Video S2. Navigation times ranged from 184 to 318 s, depending on the depth reached. On three occasions, five consecutive bifurcations were accomplished. The average time of motion per bifurcation was 35 ± 13 s, confirming that the onboard camera enabled the operator to make navigation decisions through continuous lumen visualization.

5 | Discussion

In this work, we sought to address the concerns in the scalability of magnetic soft growing robots, particularly the constraint imposed by diminishing magnetic volume [15]. Here, we demonstrate a miniaturized 7 mm system with a magnetic tip mount capable of navigating with distal dexterity around three-dimensional hoops and bronchial phantoms, while carrying onboard imaging and preserving a 3 mm tool channel. This design proves that pressurized bodies can still be controlled at smaller diameters, provided adequate magnetic volume.

Relative to existing colonoscopy models (18–25 mm D_b) [25, 26], our design accomplishes a reduced 7 mm body diameter for expanded anatomical access. Although Vine4Spine was able to reach 2 mm, its tendon-driven architecture sacrificed the workspace with low bending radius, and the integration of sensors reduced the tool channel to 0.24 mm [27]. Conversely, we preserve a 3 mm instrument channel, showing that miniaturization does not require sacrificing lumen access with an appropriate actuation mechanism and careful design.

The success of the proposed tip mount hinges on the novel integration of the IRM–ERM configuration. The systematic design study with model validation balances ease of eversion and magnetic attachment reliability, maintaining a low minimum growing pressure of ≈20 kPa, comparable to other tip mounts [23], and within clinically safe pressure ranges [32, 33]. Guiding a soft-growing robot under open-loop joystick control is typically challenging, as multiple actuation inputs must be coordinated to maintain curvature and avoid drift [10, 25, 26]. Nevertheless, the magnetic steering enables workspace angles exceeding ±90°, allowing consistent completion of consecutive 3D hoop trajectories in 189 ± 26 s. Compared to prior demonstrations of magnetic vine robots limited to planar or single-turn motion in Kim et al. [15], these results expand on the higher controllability and stability offered by magnetic actuation, suitable for complex 3D navigation.

Active steering mechanisms using tip tendon-driven mechanical and pneumatic actuators reported a bending radius of 60–200 mm, while systems utilizing distributed cPAMs, pouch motors, and fPAMs reported much larger values in the range of 220–950 mm [25]. Within the same range, the soft growing endoscope (SGE) reported a radius of 160–560 mm based on extension ratios from 8:10 to 10:10 [26]. The work by Shi et al. [25] notably went below this range to 48 mm by using a tip pneumatic soft actuator. Nevertheless, the magnetic steering presented here allows reversals with a smaller turning radius of 34 mm, consistent only with the magnetic tip presented in [15].

Our design supported navigation through five successive bifurcations up to the third generation of the bronchial tree model [34] in 184–318 s by guidance solely on the integrated 1 mm camera. Previous bronchial studies using magnetic skin (8 mm D_b) [16] reached only the second generation and had reduced workspace, limited by the EPMs' close position. More recent magnetic fluid systems (5 mm D_b) [17] reached the fourth generation in 92–140 s, but relied on duty cycling to hold tools at the tip and external camera tracking. Furthermore, the camera cable was kept external to the tool channel to reduce body friction. Instead, we integrate internal imaging without duty cycling in an average traversal time of 35 ± 13 s per bifurcation during active motion, consistent with the 24–52 s intersegmental navigation times reported in simulated bronchoscopy studies [35].

Future work will focus on exploring the use of softer materials for the ERM housing, and testing silicone-embedded permanent magnets [36] to enhance environmental compliance. Additionally, model validation will be expanded to assess its generalization across different magnet sizes and tip geometries. Moreover, we would like to implement sensors at the reserved slot. Soft force sensors at the tip that measure the effect on tissues have been utilized [37] to keep the structure compliant. Similarly, we aim to explore the integration of localization sensors to develop closed-loop control [38] by relying on both image and force feedback to achieve autonomous navigation. This feedback system can significantly reduce the time taken during visual assessment and manual command execution by eliminating human latency. Additionally, it can benefit stable stand-off distances between the EPM and the anatomy, which could mitigate the difficulty observed during open-loop teleoperation in the phantom trials. Increasing the magnetic moment of the EPM (e.g., size, remanence) could also extend the feasible actuation range.

The bronchoscopy case study remains an initial demonstration for exploring endoluminal pathways. In the future, we intend to develop a complete bronchoscopy platform that can undergo more extensive clinical validation. Further miniaturization will be necessary to access deeper regions of the lungs, which is primarily limited by the higher growing pressures required to overcome increased friction at smaller scales [39], as well as by the reduced magnetic volume available in miniature models. Other millimeter-scale soft robots [40] have already been miniaturized to 3.5 mm, reaching as far as the fourth generation of the bronchi, with sizes comparable to rigid counterparts such as Intuitive Surgical Ion and Johnson and Johnson Monarca commercial systems [41]; though, their approach still relies on traditional locomotion based on translation.

Finally, a dedicated retraction system should be explored when aiming for a complete platform. Buckling is a common problem found during vine robot retraction [42]. However, this could be mitigated by employing a magnetic wrench for body stabilization [15] or by integrating dedicated soft retraction mechanisms [26]. Ultimately, our findings suggest that magnetic tip actuation provides a scalable route to design simplification, enabling miniaturization without sacrificing steerability, visualization, or instrument access.

Acknowledgments

The authors would like to thank Nikita Greenidge and Benjamin Calme for their guidance during the experimental stages of this work. Figure 1 created in BioRender. Yanez, A. (2026) https://BioRender.com/gn189mm. This work was supported in part by the Engineering and Physical Sciences Research Council (EPSRC) under grants EP/Y037235/1, EP/V047914/1, and EP/V009818/1; the European Research Council (ERC) through the European Union's Horizon 2020 Research and Innovation Programme under grant 818045; and the National Institute for Health and Care Research (NIHR) Leeds Biomedical Research Centre (BRC) (NIHR203331). Any opinions, findings, and conclusions or recommendations expressed in this article are those of the authors and do not necessarily reflect the views of the EPSRC, the ERC, or the NIHR. J. C. was supported by the Leverhulme Trust and the Royal Academy of Engineering under the RAEng/Leverhulme Trust Research Fellowships scheme (LTRF-2425-21-154).

Funding

This work was supported by the Engineering and Physical Sciences Research Council (EP/Y037235/1, EP/V047914/1, and EP/V009818/1), European Research Council (818045), Leeds Biomedical Research Centre (NIHR203331), Royal Academy of Engineering (LTRF-2425-21-154).

Conflicts of Interest

The authors declare no conflicts of interest.

References

1. P. E. Dupont, B. J. Nelson, M. Goldfarb, et al., "A Decade Retrospective of Medical Robotics Research from 2010 to 2020," *Science Robotics* 6, no. 60 (2021): 8017.

2. S. Kim, C. Laschi, and B. Trimmer, "Soft Robotics: A Bioinspired Evolution in Robotics," *Trends in Biotechnology* 31, no. 5 (2013): 287.

3. M. Runciman, A. Darzi, and G. P. Mylonas, "Soft Robotics in Minimally Invasive Surgery," *Soft Robotics* 6, no. 4 (2019): 423.

4. E. W. Hawkes, et al., "A Soft Robot that Navigates Its Environment through Growth," *Science Robotics* 2, no. 8 (2017): 3028.

5. L. H. Blumenschein, M. M. Coad, D. A. Haggerty, A. M. Okamura, and E. W. Hawkes, "Design, Modeling, Control, and Application of Everting Vine Robots," *Frontiers in Robotics and AI* 7 (2020): 548266.

6. P. A. der Maur, B. Djambazi, Y. Haberthür, et al., "RoBoa: Construction and Evaluation of a Steerable Vine Robot for Search and Rescue Applications," in *2021 IEEE 4th International Conference on Soft Robotics (RoboSoft)*, (2021), 15–20.

7. P. Berthet-Rayne, S. M. Sadati, G. Petrou, et al., "Mammobot: A Miniature Steerable Soft Growing Robot for Early Breast Cancer Detection," *IEEE Robotics and Automation Letters* 6, no. 3 (2021): 5056.

8. L. H. Blumenschein, L. T. Gan, J. A. Fan, A. M. Okamura, and E. W. Hawkes, "A Tip-Extending Soft Robot Enables Reconfigurable and Deployable Antennas," *IEEE Robotics and Automation Letters* 3, no. 2 (2018): 949.

9. L. T. Gan, L. H. Blumenschein, Z. Huang, A. M. Okamura, E. W. Hawkes, and J. A. Fan, "3D Electromagnetic Reconfiguration Enabled by Soft Continuum Robots," *IEEE Robotics and Automation Letters* 5, no. 2 (2020): 1704.

10. M. M. Coad, L. H. Blumenschein, S. Cutler, et al., "Vine Robots: Design, Teleoperation, and Deployment for Navigation and Exploration," *IEEE Robotics and Automation Magazine* 27, no. 3 (2019): 120.

11. N. G. Kim, D. Seo, S. Park, and J. H. Ryu, "Self-Retractable Soft Growing Robots for Reliable and Fast Retraction While Preserving Their Inherent Advantages," *IEEE Robotics and Automation Letters* 9, no. 2 (2024): 1082.

12. N. D. Naclerio, E. W. Hawkes, and Simple, Low-Hysteresis, Foldable, Fabric Pneumatic Artificial Muscle," *IEEE Robotics and Automation Letters* 5, no. 2 (2020): 3406.

13. J. D. Greer, T. K. Morimoto, A. M. Okamura, and E. W. Hawkes, "Series pneumatic artificial muscles (sPAMs) and application to a soft continuum robot," in *IEEE International Conference on Robotics and Automation (ICRA)*, (2017), 5503–5510.

14. T. Abrar, F. Putzu, J. Konstantinova, and K. Althoefer, "EPAM: Eversive pneumatic artificial muscle," in *IEEE International Conference on Soft Robotics (RoboSoft)*, (2019), 19–24.

15. N. G. Kim, N. J. Greenidge, J. Davy, et al., "External Steering of Vine Robots via Magnetic Actuation," *Soft Robotics* 12, no. 2 (2025): 159.

16. J. Davy, et al., "Vine Robots with Magnetic Skin for Surgical Navigations," *IEEE Robotics and Automation Letters* 9, no. 8 (2024): 1–8.

17. J. Davy, T. P. Dean, N. J. Greenidge, et al., "Magnetic Fluid-Driven Vine Robots for Minimally Invasive Tissue Biopsy Sampling," *Advanced Intelligent Systems* 7 (2025): 2400827.

18. C. Watson and K. Morimoto, "Permanent Magnet-Based Localization for Growing Robots in Medical Applications," *IEEE Robotics and Automation Letters* 5, no. 2 (2020): 2666.

19. J. D. Greer, T. K. Morimoto, A. M. Okamura, and E. W. Hawkes, "A Soft, Steerable Continuum Robot That Grows via Tip Extension," *Soft Robotics* 6, no. 1 (2019): 95.

20. D. Mishima, T. Aoki, and S. Hirose, "Development of a Pneumatically Controlled Expandable Arm for Rescue Searches in Tight Spaces," *International Journal of Robotics Research* 25, no. 1 (2006): 103.

21. J. H. Kim, J. Jang, S. M. Lee, S. G. Jeong, Y. J. Kim, and J. H. Ryu, "Origami-Inspired New Material Feeding Mechanism for Soft Growing Robots to Keep the Camera Stay at the Tip by Securing Its Path," *IEEE Robotics and Automation Letters* 6, no. 3 (2021): 4592.

22. C. Suulker, S. Skach, D. Kaleel, et al., "Soft Cap for Vine Robots," in *IEEE International Conference on Intelligent Robots and Systems (IROS)*, (2023), 6462–6468.

23. S. G. Jeong, M. M. Coad, L. H. Blumenschein, et al., "A Tip Mount for Transporting Sensors and Tools using Soft Growing Robots," in *IEEE International Conference on Intelligent Robots and Systems (IROS)*, (2019), 8781–8788.

24. J. Luong, P. Glick, A. Ong, et al., "Eversion and retraction of a soft robot towards the exploration of coral reefs," in *IEEE International Conference on Soft Robotics (RoboSoft)*, (2019), 801–807.

25. J. Shi, K. Borvorntanajanya, K. Chen, E. Franco, and F. R. Y. Baena, "Design, Control and Evaluation of a Novel Soft Everting Robot for Colonoscopy," *IEEE Transactions on Robotics* 41 (2025): 1–17.

26. N. G. Kim, S. Park, D. Seo, et al., "A Soft Growing Robotic Endoscope for Painless and Strain-Free Insertion," *Soft Robotics* (2025).

27. Z. Wu, S. H. Sadati, P. Vartholomeos, et al., "2025 IEEE/RSJ International Conference on Intelligent Robots and Systems (IROS)," *Vine4Spine: A Steerable Tip-Growing Robot with Contact Force Estimation for Navigation in the Spinal Subarachnoid Space* (2025): 17279–17286.

28. S. A. Harthy, S. M. Sadati, C. Girerd, et al., "Tip-Growing Robots: Design, Theory, Application," *IEEE Transactions on Robotics* 41 (2025) 5511–5532.

29. M. McCandless, A. Perry, N. DiFilippo, et al., "A Soft Robot for Peripheral Lung Cancer Diagnosis and Therapy," *Soft Robotics* 9, no. 4 (2022): 754.

30. L. H. Blumenschein, A. M. Okamura, and E. W. Hawkes, "*Modeling of Bioinspired Apical Extension in a Soft Robot*," In 2017 (Conference on Biomimetic and Biohybrid Systems, 2017): 10384 LNCS 522.

31. M. Ortner and L. G. Coliado Bandeira, "Magpylib: A Free Python Package for Magnetic Field Computation," *SoftwareX* 11 (2020): 100466.

32. V. Pathak, I. Welsby, K. Mahmood, M. Wahidi, N. MacIntyre, and S. Shofer, "Ventilation and Anesthetic Approaches for Rigid Bronchoscopy," *Annals of the American Thoracic Society* 11, no. 4 (2014): 628.

33. Y. Li, J. Peine, M. Mencattelli, J. Wang, J. Ha, and P. E. Dupont, "A Soft Robotic Balloon Endoscope for Airway Procedures," *Soft Robotics* 9, no. 5 (2022): 1014.

34. M. Chovancová and J. Elcner, "The Pressure Gradient in the Human Respiratory Tract," in *EPJ Web of Conferences*, 67 (2014): 02047.

35. K. O. Agbontaen, K. M. Cold, D. Woods, et al., "Artificial Intelligence-Guided Bronchoscopy Is Superior to Human Expert Instruction for the Performance of Critical-Care Physicians: A Randomized Controlled Trial," *Critical Care Medicine* 53, no. 5 (2025): e1105.

36. G. Pittiglio, J. H. Chandler, T. da Veiga, et al., "Personalized Magnetic Tentacles for Targeted Photothermal Cancer Therapy in Peripheral Lungs," *Communications Engineering* 2, no. 1 (2023): 1.

37. K. Borvorntanajanya, J. Shi, J. F. Ahmed, E. Franco, and F. R. Y. Baena, "A Pneumatic Force Sensor for Enhanced Force Feedback in Robotic Colonoscopy," *IEEE Transactions on Medical Robotics and Bionics* 7, no. 4 (2025): 1377–1388.

38. A. Z. Taddese, P. R. Slawinski, M. Pirotta, E. De Momi, K. L. Obstein, and P. Valdastri, "Enhanced Real-Time Pose Estimation for Closed-Loop Robotic Manipulation of Magnetically Actuated Capsule Endoscopes," *International Journal of Robotics Research* 37, no. 8 (2018): 890.

39. C. Girerd, A. Alvarez, E. W. Hawkes, and T. K. Morimoto, "Material Scrunching Enables Working Channels in Miniaturized Vine-Inspired Robots," *IEEE Transactions on Robotics* 40 (2024): 2166.

40. D. Van Lewen, T. Janke, H. Lee, R. Austin, E. Billatos, and S. Russo, "A Millimeter-Scale Soft Robot for Tissue Biopsy Procedures," *Advanced Intelligent Systems* 5 (2023): 5.

41. A. J. Kent, K. A. Byrnes, and S. H. Chang, "State of the Art: Robotic Bronchoscopy," *Seminars in Thoracic and Cardiovascular Surgery* 32, no. 4 (2020): 1030.

42. S. Kim and T. K. Morimoto, "Kinked Air Channel Enables Retraction of Small-Scale Soft Everting Robots," in *IEEE 8th International Conference on Soft Robotics (RoboSoft)*, (2025).

Supporting Information

Additional supporting information can be found online in the Supporting Information section.